Performance investigation of adsorption cooling and desalination systems employing thermally enhanced copper foamed bed coated with SAPO-34 and CPO-27(Ni)

Mohamed Shaaban[1], Mahmoud Badawy Elsheniti[2,1*], Ahmed Rezk[3,4], Mohamed Elhelw[1], Osama A. Elsamni[1]

[1]Mechanical Engineering Department, Faculty of Engineering, Alexandria University, Alexandria 21544, Egypt.
[2]Mechanical Engineering Department, College of Engineering, King Saud University, Riyadh 11451, Saudi Arabia
[3]Energy and Bioproducts Research Institute (EBRI), College of Engineering and Physical Science, Aston University, Birmingham, UK, B4 7ET
[4]Aston Institute of Material Research (AIMR), College of Engineering and Physical Science, Aston University, Birmingham, UK, B4 7ET

*Corresponding author: Mahmoud Elsayed Badawy Elsheniti,
mbadawy.c@ksu.edu.sa; melsheniti@gmail.com

Abstract

Despite the increasing interest in adsorption cooling and desalination systems, the poor heat hence mass transfer in the adsorbent-bed (the core component) impedes the efficient energy conversion at the system level and increases its physical footprint. In response, this paper numerically investigates the overall enhancement of adsorption cooling cum desalination system employing emerging copper foamed adsorbent beds of advanced thermal performance coated with advanced adsorbent materials to address such an untapped challenge. Silico-aluminophosphate (SAPO-34) and Nickel-based metal-organic framework CPO-27(Ni) adsorbents were employed. First, a 2-D axisymmetric computational fluid dynamic fully coupled model was developed to simulate the adsorbent-beds considering non-ideal condenser and evaporator pressures. Second, the influence of different operating conditions and copper foam thicknesses was investigated at the adsorbent-bed and system levels. The advanced adsorption kinetics of SAPO-34 enabled shortening the cycle time from 600 to 180 s, which enhanced the coefficient of performance (COP), specific cooling power (SCP), and specific daily water production (SDWP) of the system by 163%, 223%, and 228%. The regeneration temperature was the most influential parameter on the systems' performance within the investigated range (70-100 °C). It enhanced the COP from 0.2 to 0.421, SCP from 132 to 821 $W.kg^{-1}$, and SDWP from 4.7 to 29.3 $m^3.ton^{-1}.day^{-1}$, for CPO-27(Ni) coated bed; and COP from 0.378 to 0.388 and SCP from 393 to 855 $W.kg^{-1}$ and SDWP from 14 to 31 $m^3.ton^{-1}.day^{-1}$, for SAPO-34 coated bed. The reported enhancements at the adsorption system-level signpost metal-foamed adsorbent-bed coating the most thermally efficient adsorbent-bed design.

Keywords: Adsorption chiller; Copper foam coating; Adsorption desalination; Advanced adsorbents; MOF CPO-27(Ni); AQSOA^{TM} FAM-Z02.

Highlights

- CPO-27(Ni) and SAPO-34 coated on foamed adsorption beds are numerically simulated
- Comparative studies on the two adsorbents are introduced at a two-bed system level
- Adsorption kinetics of SAPO-34 advances its system performance above CPO-27(Ni)
- Using thicker coated foam enhances the COP of both adsorbent systems noticeably

1 Introduction

Adsorption cooling cum desalination (ACD) systems, the most feasible way to decarbonize cooling and desalination production processes, have gained increasing attention via enormous investigations in the last two decades [1]. Using water as a natural refrigerant of zero global warming and ozone depletion indices raises such emerging systems' significance. Besides, producing potable water and the by-product of cooling in ACD enhances the overall energy efficiency of such systems. Moreover, low-temperature waste and renewable heat resources (55- 100 °C) can be adequately used to drive the ACD systems [2, 3], which enhances diversifying the energy mix for many countries of the immense need for cooling and desalination [4, 5]. Nevertheless, the inherited low performance of ADC determined by specific cooling power (SCP), coefficient of performance (COP), and daily water production (DWP) of current ACD systems increase the initial cost and physical footprint compared to the conventional systems. The low performance of ACD is stemmed from the inefficient heat transfer hence mass transfer within the adsorbent materials due to their low effective thermal agility. As a result, the system's response to the temperature variations during exothermic adsorption and endothermic desorption swing is delayed [6]. Many approaches were investigated to enhance ACD systems to compete with other conventional systems, such as using new composite materials [7-11], adding metallic additives of higher thermal conductivity than the adsorbent materials [12-14], developing new granulated adsorbent packing techniques [15], using wire finned heat exchangers [16, 17], and adsorbent coating [18-21].

Among the different approaches, adsorbent coating showed the most reduction in the thermal contact resistance [22]. There are various adsorbent coating approaches, each of which has its merits. One approach is binding the adsorbent grains directly on the surface of the adsorbent-bed heat exchanger using epoxy or organic glue; despite the significant reduction of the contact resistance, it inhibits the mass transfer due to the low vapor permeability within the adsorbent material domain [22-24]. Another coating approach is the direct synthesis of thin adsorbent coatings on the heat exchanger surface. It enhances heat transfer due to nearly perfect adhesion; nevertheless, it reduces the mass transfer to some extent and increases the volume of the sorption bed to accommodate the critical mass of adsorbents [25-27].

There has been an emerging interest in metal foam coating [22, 28]. Using metal foam can address the downside of mass transfer caused by poor permeability in conventional coating techniques, owing to the high surface area of the foam cavities. Moreover, the thickness of the foamed structure could be increased while maintaining its mechanical strength. Furthermore, it was reported that metal foam is versatile and could be

machined without affecting its dynamic performances [29-31]. Such merits foster its feasibility for adsorption systems application to address the heat transfer simultaneously with the mass transfer challenges and withstand the thermal stresses developed from the intense temperature swing during the intermittent adsorption/desorption processes.

Many studies have paved the way to apply metal foams in the adsorption systems by proving their reliability. Calabrese et al. [32] verified the stability of SAPO-34-silicone composite foams at different SAPO-34 contents by applying 1500 ageing cycles. Calabrese et al. [24] studied a synthesized composite made of SAPO-34 filled silicone foam for adsorption heating and cooling applications, demonstrating a higher COP without affecting its mechanical performance and maximum uptake. Bauer et al. [33] reported the potential improvement of the performance of adsorption systems when metal foam hosted CaCl2/silica gel composite, AlPO, and SAPO zeolites. Calabrese et al. [34] suggested using novel silicone-SAPO-34 composite materials for heat storage applications after investigating the morphological aspects, water adsorption, and mechanical properties at various SAPO-34 contents. Bonaccorsi et al. [35] used cellular graphite foam of porosity 85% as porous structures for direct synthesis of SAPO-34 zeolite and reached a thermal conductivity of 24 $W.m^{-1}.K^{-1}$.

For further investigating the impact of the metal foam on the adsorption systems' performance, Xu et al. [36] experimentally studied copper foam cured MIL-101 (CFCM). The thermal conductivity was 0.8624 $Wm^{-1}K^{-1}$, which was 14 times higher than that of the powder form. It enhanced the cooling capacity, SCP, and volumetric cooling power (VCP) by 1.8, 2.6, and 4 times, respectively, compared to the system employed granular packed bed. Hu et al. [37] numerically studied a single bed of composite zeolite/aluminium foam, which enhanced SCP by 200 % and COP by 37 % compared to a packed bed. Freni et al. [22] experimentally determined the porosity and the permeability of copper foams coated with zeolite, coupled with a mathematical model to predict the performance of one-bed adsorption cooling system. The enhancements of SCP and VCP were 510 % and 548 %, respectively, compared to loose pellets. Mohammed et al. [38] investigated the use of silica-gel granules packed into a high-porosity aluminium foam. The SCP, VCP, and COP were enhanced by 161 %, 137 %, and 9 %, respectively. Pinheiro et al. [31] developed a 2-D numerical model to simulate the performance of a one-bed heat pump adsorption system using copper foams coated with two adsorbent materials. The metal organic framework (MOF) CPO-27(Ni) performance was benchmarked against SAPO-34; the latter adsorbent outperformed the former, where the $COP_{heating}$, the specific heating power, and the volumetric heat power were improved by 21%, 34%, and 17%, respectively.

AQSOA^{TM} FAM-Z02 is a new type of zeolite, otherwise dubbed silico-aluminophosphate (SAPO-34), of exceptional adsorption characteristics. It shows adsorption isotherm type V with an uptake up to 0.25 $kg_w.kg_{sads}^{-1}$ within a narrow range of low relative pressure and low desorption temperature (60 - 100 °C) and relatively high kinetics [39-41]. CPO-27(Ni) is an isostructural MOF material produced of high porous surface area and high-water adsorption uptake (0.47 $kg_w.kg_{ads}^{-1}$). It shows adsorption isotherm type I and reaches 81%

of its adsorption capacity at a low relative pressure (~0.05), which is of great benefit in cooling and water desalination applications [42, 43].

Given the current literature, the thermal performance of adsorbent beds utilizing metal foams coated with emerging adsorbents and their influence on the system's performance is yet to be understood. Therefore, the study aims to undertake a comparative study on the thermal performance of coating SAPO-34 and CPO-27(Ni) as emerging adsorbents on copper foamed heat exchangers at the adsorbent-bed and system levels. The aim of the study was achieved through two objectives: (i) developing a 2-D axisymmetric CFD model using COMSOL Multiphysics to simulate the adsorbent-beds, considering the actual instantaneous pressure to replicate boundary conditions during adsorption/evaporation and desorption/condensation, and (ii) investigating the effects of different operating conditions and copper foam thicknesses at the adsorbent-bed and system levels. This work's novelty lies in correlating the advanced performance of emerging adsorbent materials coated onto copper foamed-bed to the overall performance of adsorption cooling and desalination systems. The investigated adsorbents and the range of physical and operating conditions are the critical contributions that help addresses the poor performance of the adsorption cooling and desalination systems by developing advanced adsorbent-bed designs.

Nomenclature:

ACD	Adsorption cooling cum desalination	Q_m	Source term in mass balance equation (m^2)
COP	Coefficient of performance $(-)$	Q_{ads}	Isosteric heat of adsorption at half coverage $(J.kg^{-1})$
C_p	Specific heat capacity $(J.kg^{-1}.K^{-1})$	Q_{st}	Isosteric heat of adsorption at zero su face coverage $(J.kg^{-1})$
D_s	Surface diffusivity $(m^2.s^{-1})$	R_w	Specific gas constant $(J.kg^{-1}.k^{-1})$
D_{so}	Pre-exponent constant of surface diffusivity $(m^2.s^{-1})$	$\mathcal{R}$	Universal gas constant $(J.mol^{-1}.k^{-1})$
E_a	The activation energy of surface diffusion $(J.mol^{-1})$	R	Radius (m)
HTF	Heat transfer fluid	$SDWP$	Specific daily water production $(m^3.ton^{-1}.day^{-1})$
k	Thermal conductivity $(W.m^{-1}.K^{-1})$	T	Temperature (K)
k_T	Thermal turbulent conductivity $(W.m^{-1}.K^{-1})$	t	Time (s)
k_p	Bed permeability (m^2)	UA	Heat transfer conductance $(W.K^{-1})$
K_{LDF}	Mass transfer coefficient (s^{-1})	u	Fluid velocity (m/s)
LH	Latent heat $(J.kg^{-1})$	VCP	Volumetric cooling capacity $(W.L^{-1})$
M	Mass (kg)	V_{AHEx}	Total volume of heat exchanger (L)
n	Number of cycles per day	W	Uptake $(kg_w.kg_{ad}^{-1})$
N_{tube}	Number of tubes per bed	W_{eq}	Equilibrium adsorption uptake $(kg_w.kg_{ad}^{-1})$
p	Pressure (Pa)		

Greek symbols:

δ	Adsorbent thickness (m)
ρ	Density $(kg.m^{-3})$
μ	Dynamic viscosity $(Pa.s)$
μ^T	Turbulent dynamic viscosity $(Pa.s)$
ε_b	Bed porosity $(-)$
ε	Effectiveness $(-)$
ζ	Volume fraction of the copper foam $(-)$

Subscripts:

ads	Adsorbent
a	Adsorbate
AHEx	Adsorption heat exchanger
b	Bed
coat	Adsorbent coating
cw	Cooling water
chw	Chilled water
cond	Condenser
eff	Effective
eva	Evaporator
eq	Equilibrium
f	Fluid
fo	Copper foam
hw	Heating water
i	Inlet
init	Initial
LDF	Linear driving Force
met	Metal
out	Outlet
rl	Refrigerant liquid
rv	Refrigerant Vapor
s	Solid Adsorbent
sat	Saturation
v	Vapor
w	water

2 System description

A conventional configuration of a two-bed ACD system was utilized to evaluate the performance of two adsorbent materials coated on copper foams: namely CPO-27(Ni) and SAPO-34. The copper foams are formed on the outer surface of plain copper tubes typically used to transfer the thermal energy to/from the heat-transfer-fluid (HTF) during the adsorption/desorption processes in the adsorbent-beds. The system layout and its main components employed for numerical modelling are illustrated in Fig. 1. Each bed undergoes four cyclic phases: pre-heating, heating (desorption), pre-cooling, and cooling (adsorption), following a timing strategy for interconnecting and the HTF control valves. Water is used as an adsorbate, which adsorbs the clean water from the saline water, previously fed to the evaporator, using the evaporation process while producing cooling. More details about the operational theory of the two-bed adsorption system used for cooling and desalination can be obtained in references [2, 44].

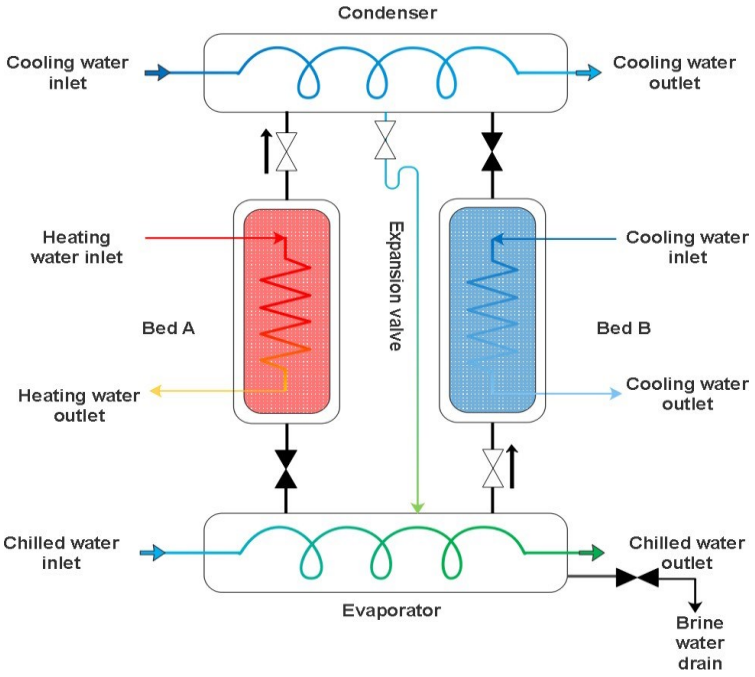

Fig. 1. Schematic diagram of a two-bed adsorption cooling and desalination system.

3 Mathematical modelling

A 2-D axisymmetric transient fully-coupled model was developed for the two adsorbent materials, considering four domains: HTF, plain tube, adsorbent coated on copper foams (foam-based adsorbent domain), and vacuum space domains, as shown in Fig. 2. The model merged the physical and thermal characteristics of the copper foams and the adsorbent coated layers via volume averaged approach in mass, momentum, and energy conservation equations. The isotherms and kinetics models for the two adsorbents were integrated with the conservation equations. Zero-dimensional models considering the energy balances and heat transfer effectiveness limits for both condenser and evaporator components were applied at the valve openings of each bed as boundary conditions. The present model can observe the temporal and the local variations of the variables such as temperature, pressure, and the amount of adsorbate within the adsorbent bed. The governing equations were solved simultaneously, considering the ACD system's independence of the initial conditions, determined after reaching the cyclic steady-state operation.

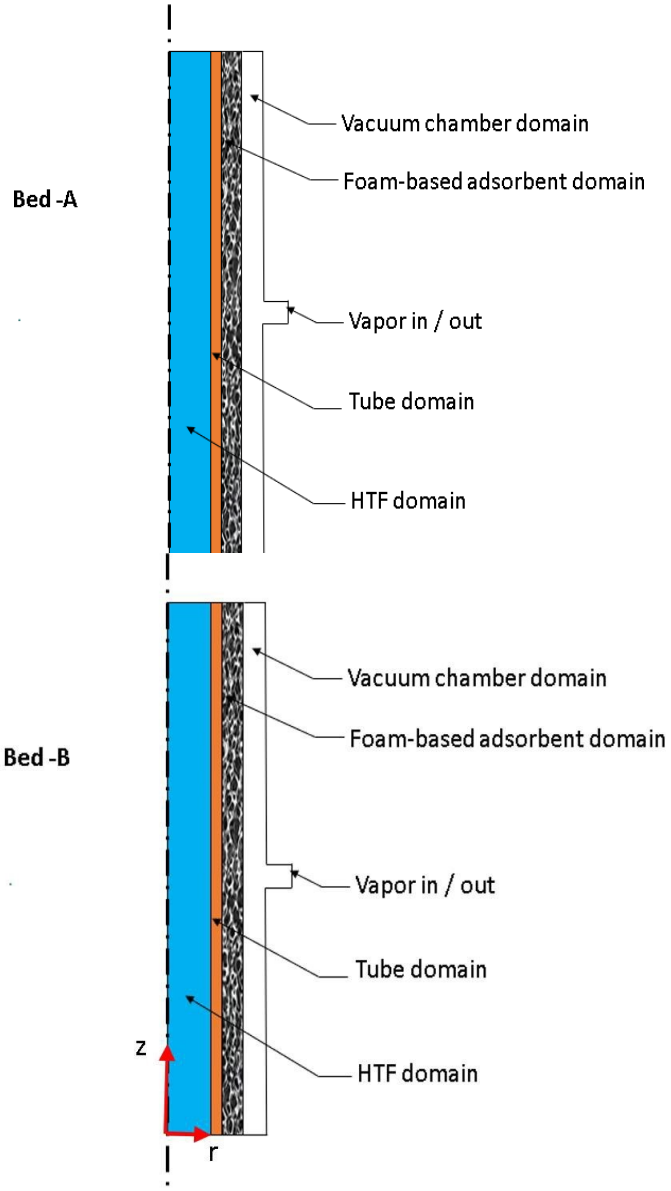

Fig. 2. The 2-D axisymmetric representative adsorbent bed tubes

3.1 Assumptions

COMSOL Multiphysics was employed to solve the governing equations simultaneously while considering the following assumptions [23, 31, 45-47].

1) Water in the vapor phase acts as an ideal gas.

2) The bed porosity is assumed to be isotropic.

3) Thermal contact resistance is eliminated between the adsorbent coating and the copper foam.

4) The thermal conductivity of the composite bed is considered to be that of copper foam effective thermal conductivity.

5) Local thermal equilibrium is assumed between the adsorbent, the adsorbed water, and the water vapor.

6) Beds' containers are well insulated, so there are no heat losses across the outer boundaries.

3.2 Governing equations

3.2.1 Heat transfer fluid

The conservation of mass for incompressible fluid flow inside the tube:

$$\rho_f \nabla . u_f = 0 \quad (1)$$

The turbulence model used in the study was the k-ε model, which introduces two additional transport equations solved for two dependent variables: the turbulent kinetic energy (κ) and the dissipation rate of turbulence energy (ε). The wall functions modified the model to increase its near wall accuracy. The wall functions in COMSOL were assumed to start a distance from the wall. The k-ε model converges relatively fast in this study, and the results showed a good agreement with the experimental data published by Elsheniti et al. [45]. For turbulent flow, the RANS equation 2 was used.

$$\rho_f \frac{\partial u_f}{\partial t} + \rho_f u_f . (\nabla u_f) = -\nabla p_f I + \nabla . [(\mu + \mu_T)(\nabla u_f + (\nabla u_f)^T) - \frac{2}{3}\rho_f \kappa I] \quad (2)$$

The energy conservation considering the enhancement in the thermal conductivity due to the turbulent flow (k_T) was governed by equation 3 [45]:

$$\rho_f C_{p,f} \frac{\partial T_f}{\partial t} + \nabla . (\rho_f C_{p,f} u_f T_f) - \nabla . ((k_f + k_T)\nabla T_f) = 0 \quad (3)$$

3.2.2 Heat transfer tube

The energy conservation of the metal tubes, considering conduction mode only, was governed by equation 4.

$$\rho_{met} C_{p,met} \frac{\partial T_{met}}{\partial t} - \nabla . (k_{met} \nabla T_{met}) = 0 \quad (4)$$

3.2.3 Adsorbent material

The adsorbate mass balance in the foam-based adsorbent domain was governed by equation 5, following Pinheiro et al. [31]:

$$\varepsilon_b \frac{\partial \rho_v}{\partial t} + (1 - \varepsilon_b)(1 - \zeta)\rho_s \frac{\partial W}{\partial t} + \nabla . (\rho_v u) = 0 \quad (5)$$

Herein $\varepsilon_b$is the bed porosity, ζ is the volume fraction of the copper foam, W is the instantaneous amount of the adsorbate (water), ρ_v is the vapor density, ρ_s is the adsorbent density, and u the volume-averaged vapor velocity vector. Equation 6 can be used to govern the momentum of the vapor flow.

$$\frac{\rho_v}{\varepsilon_b}\left[\frac{\partial u}{\partial t} + \frac{1}{\varepsilon_b} u . (\nabla u)\right] = \nabla\left[-pI + \frac{\mu}{\varepsilon_b}(\nabla u + (\nabla u)^T) - \frac{2}{3}\frac{\mu}{\varepsilon_b}(\nabla . u)I\right] - \left[\frac{\mu}{k_p} + \frac{Q_m}{\varepsilon_b^2}\right]u \quad (6)$$

This form of the modified Navier-Stokes equations describes the homogenous fluid flow in isotropic porous media considering the effect of mass desorbed or adsorbed on the momentum balance [45, 48]. In addition, this form enables the coupling with the typical Navier-Stokes equations solved for the vacuum space at the interface with the composite foam-adsorbent domain. Equation 7 determines Q_m as a function of porosity, volume fraction and the rate of adsorption/desorption ($\frac{\partial W}{\partial t}$).

$$Q_m = -(1 - \varepsilon_b)(1 - \zeta)\rho_s \frac{\partial W}{\partial t} \quad (7)$$

Equation 8 presents the energy balance for the composited foam-adsorbent domain.

$$\frac{\partial}{\partial t}((\rho C_p)T) + \nabla(\rho_v u C_{p,v} T) = \nabla . (k_{eff,bed} \nabla T) + (1 - \varepsilon_b)(1 - \zeta)\rho_s Q_{ads} \frac{\partial W}{\partial t} \quad (8)$$

The term ρC_p is the total heat capacity of the foam-adsorbent domain considering all the materials present in the control volume: metal foams, adsorbent, adsorbate, and water molecules. It can be determined as shown in equation 9.

$$\rho C_p = (1 - \varepsilon_b)(1 - \zeta)\rho_s(C_{p,s} + W\, C_{p,a}) + \varepsilon_b\, \rho_v C_{p,v} + (1 - \varepsilon_b)\, \zeta\, \rho_{fo} C_{p,fo} \quad (9)$$

Q_{ads} is the heat of sorption. The composited bed thermal conductivity is considered as the effective thermal conductivity of the copper foam ($k_{eff,bed} = k_{foam}$), which considered the porosity of the foam structure and the vapor thermal conductivity that fills the voids that can be obtained from Equation 10 [22, 49, 50].

$$k_{eff,bed} = 0.35[\varepsilon_b\ k_v + (1 - \varepsilon_b)k_{copper}] + \frac{0.65}{(\frac{\varepsilon_b}{k_v} + \frac{1 - \varepsilon_b}{k_{copper}})} \quad (10)$$

Given that the thickness of the coated layer of the adsorbent material on the foam structure is very small (0.01 mm), and the foam cell structure (copper foams) is continuously connected under the coated layer. Therefore, the heat diffusion by conduction through the foam thickness (2 mm to 15 mm in this study) depends mainly on the foam structure conductivity. At any point in the domain, the coated layer takes the temperature of the adherent foam cell side, while the effect of thermal resistance of the heat transfer across the coated layer (0.01 mm) has minimal effect on the temperature of the coated layer, which can be neglected[22, 28, 31].

3.2.4 Vacuum chamber

The typical conservation equations for laminar incompressible flow are employed in this study to describe the vapor flow surrounding the foam-adsorbent domain in the vacuum space. The mass balance for the vapor flow can be determined using equation 11.

$$\frac{\partial \rho_v}{\partial t} + \nabla(\rho_v u) = 0 \quad (11)$$

The momentum balance can be governed by equation 12.

$$\rho_v \frac{\partial u}{\partial t} + \rho_v\ u.\nabla\,(u) = -\nabla p I + \nabla.[\,\mu\,(\nabla u + (\nabla u)^T) - \tfrac{2}{3}\,\mu(\nabla.u)\,I] \quad (12)$$

The energy balance can be governed by equation 13.

$$\frac{\partial(\rho_v C_{p,v} T_v)}{\partial t} + \nabla.(\rho_v u C_{p,v} T_v) - \nabla.(k_v \nabla T_v) = 0 \quad (13)$$

3.2.5 Evaporator model

The evaporator's thermal mass and the heat transfer effectiveness contribute to the evaporating temperature hence the evaporation pressure. In addition, the rate of adsorbed mass to the connected bed from the evaporator also affects the evaporating temperature, even with a fixed entering chilled water temperature. Therefore, energy balance for the evaporator component and its effectiveness can be governed by equations 14-15:

$$[M_{eva,rl}C_{p,eva,rl} + M_{eva,met}C_{p,eva,met}]\frac{dTeva}{dt} = \dot{m}_{chw}C_{p,chw}\varepsilon_{eva}(T_{chw,i} - T_{eva}) - (1-\alpha)\,\dot{m}_{v,eva}N_{tube,adsorber}\,[LH_{eva} - C_{p,rl}(T_{cond} - T_{eva})] \quad (14)$$

$$\varepsilon_{eva} = 1 - exp(\frac{-UAeva}{\dot{m}_{chw}C_{p,chw}}) \quad (15)$$

3.2.6 Condenser model

Similarly, the condenser thermal mass, the heat transfer effectiveness, and the rate of desorbed mass in the connected bed to the condenser are used to determine the condenser pressure in this study. Therefore, the energy balance for the condenser and its effectiveness can be determined by equations 16-17.

$$[M_{cond,rl}C_{p,cond,rl} + M_{cond,met}C_{p,cond,met}]\frac{dTcond}{dt} = -\dot{m}_{cw}C_{p,cw}\varepsilon_{cond}(T_{cond} - T_{cw,i}) + (1-\beta)\dot{m}_{v,cond}N_{tube,adsorber}[LH_{cond} + C_{p,rv}(T_{v,out} - T_{cond})] \quad (16)$$

$$\varepsilon_{cond} = 1 - exp(\frac{-UAcond}{\dot{m}_{cw}C_{p,cw}}) \quad (17)$$

The flags α and β are used in the switching times to simulate the conditions of interconnecting valves between the adsorbent beds, condenser and evaporator depending on the operating modes: adsorption/evaporation, desorption/condensation, pre-heating or pre-cooling.

3.2.7 Adsorption equilibrium and kinetics

The linear driving force model is used to determine the internal mass transfer resistance for water adsorption, as shown in equation 18 [51]:

$$\frac{\partial W}{\partial t} = K_{LDF}(W_{eq} - W) \quad (18)$$

where K_{LDF} is the overall mass transfer coefficient determined using equation 19 [49]:

$$K_{LDF} = \frac{3D_s}{\delta_{coat}^2} \quad (19)$$

where δ_{coat} is the adsorbent coating thickness and D_s parameter can be determined by Arrhenius equation 20.

$$D_s = D_{so}exp(\frac{-E_a}{\mathcal{R}T}) \quad (20)$$

D_{so} is the pre-exponent constant, E_a is the activation energy, $\mathcal{R}$ is the universal gas constant, and T is the local temperature. The equilibrium adsorption uptake (W_{eq}) can be determined using adsorption equilibrium models given developed by Wei et al. and Elsayed et al. for the used adsorbents [41, 52]. Equations 21-22 is the equilibrium isotherms for CPO-27(Ni)/water.

$$W_{eq} = 0.462248\exp[-(\frac{A}{10019.2})^4] \quad (21)$$

$$A = RT\ ln(\frac{Psat}{p}) \quad (22)$$

Equations 23-24 is the equilibrium isotherms for SAPO-34/water.

$$W_{eq} = 0.29[\frac{\mathcal{K}(\frac{p}{p_{sat}})^{1..01}}{1+(\mathcal{K}-1)(\frac{p}{p_{sat}})^{1.01}}] \quad (23)$$

$$\mathcal{K} = 7 \times 10^{-6}\exp[1.01(Q_{st} - \nabla H_v)/(R_wT)] \quad (24)$$

The adsorption isotherms of the CPO-27 (Ni) and SAPO-34 at various heating temperatures are shown in Fig. 3.

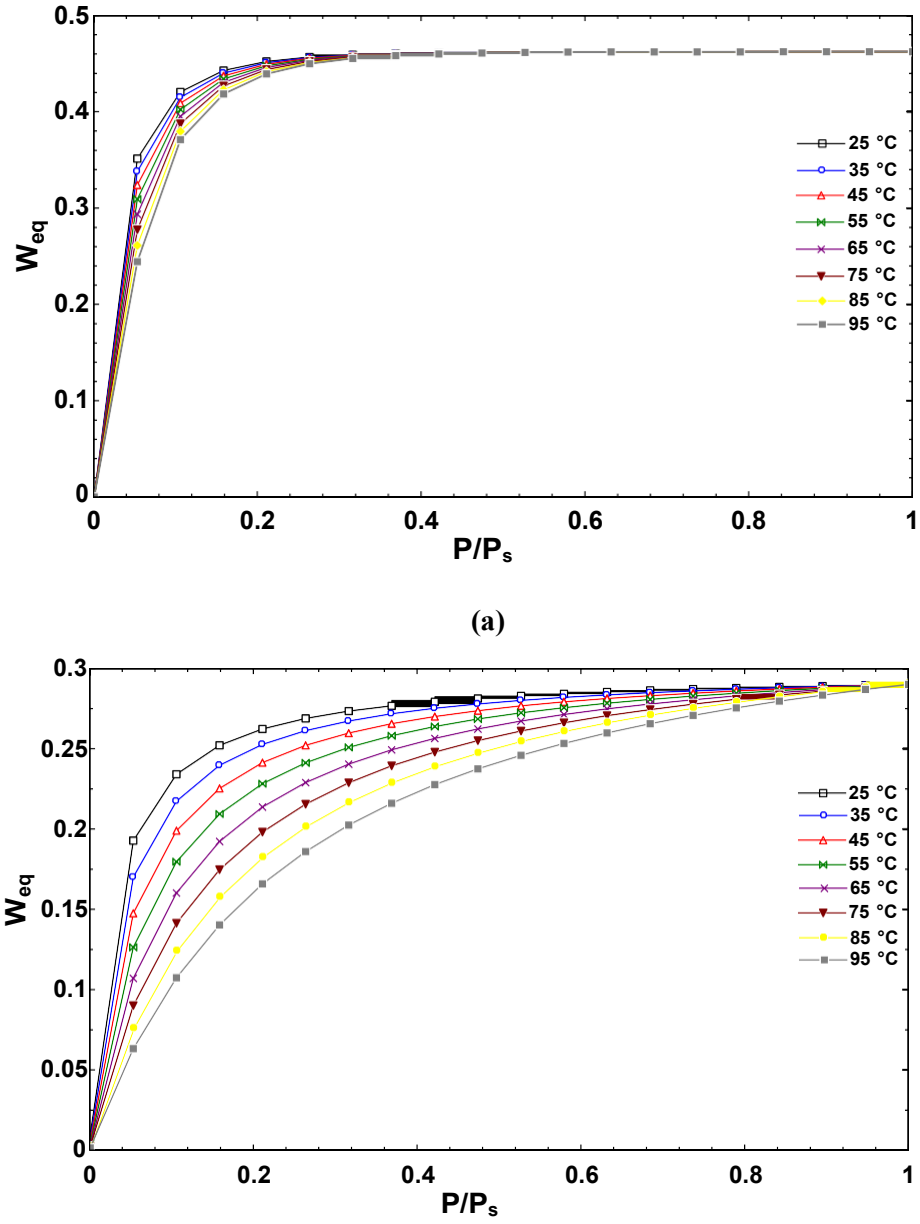

(a)

Fig. 3. Water adsorption isotherm at different temperatures (a) CPO-27 (Ni) (b) SAPO-34

3.3 Performance indicators

The cooling and desalination system performance using the two adsorbents coated on copper foams were evaluated in terms of the coefficient of performance (COP), the specific cooling power (SCP), the volumetric cooling power (VCP) and the specific daily water production ($SDWP$) as follows:

$$Q_{eva} = \frac{1}{t_{cycle}} \int_0^{t_{cycle}} \dot{m}_{chw} C_{chw} (T_{chw,i} - T_{chw,out}) dt \quad (25)$$

$$Q_{heat} = \frac{1}{t_{cycle}} \int_0^{t_{cycle}} \dot{m}_{hw} C_{hw} (T_{hw,i} - T_{hw,out}) dt \quad (26)$$

$$COP = \frac{Qeva}{Q_{heat}} \quad (27)$$

$$SCP = \frac{Qeva}{M_S} \tag{28}$$

$$VCP = \frac{Qeva}{V_{AHEx}} \tag{29}$$

$$SDWP = \sum_{0}^{n} \int_0^{t_{cycle}} \frac{\dot{m}_{chw} C_{chw} (T_{chw,i} - T_{chw,out})}{(h_{fg} - C_{p,w}(T_{cond} - T_{eva})) * M_s} \, dt \tag{30}$$

The V_{AHEx} is the total volume of the adsorption heat exchanger, M_s is the total amount of adsorbent in the two beds, and n is the number of cycles per day. The thermophysical properties, isotherms parameters, physical and operational parameters used in the computational solver were obtained from work published by Pinheiro et al. [31] and furnished in Table 1. The parameters used for the condenser and the evaporator components were obtained from work published by Elsheniti et al. [45] and populated in Table 2. The overall heat transfer coefficients for both the condenser and evaporator were calculated based on well-established correlations in the heat transfer for shell and tube condenser in which the cooling water flowed inside the tube and flooded type shell-and-tube evaporator. The labels used to describe the dimensional parameters of a foamed adsorption tube are shown in Fig. 4.

Table 1. Values adopted in simulating the baseline model.

Parameter	Value		SI Unit
Main properties			
	CPO-27(Ni)	**SAPO-34**	
Specific heat of adsorbent ($C_{p,s}$)	1000	892	$(J.kg^{-1}.k^{-1})$
Adsorbent density (ρ_s)	2600	2260	$(kg.m^{-3})$
Pre-exponent constant (D_{so})	4.9×10^{-9}	3.92×10^{-6}	$(m^2.s^{-1})$
Activation energy (E_a)	25125	28035	$(J.mol^{-1})$
Isosteric heat of adsorption at half coverage (Q_{ads})	2.881×10^6	3.160×10^6	$(J.kg^{-1})$
Isosteric heat of adsorption at zero surface coverage (Q_{st})	------	4.560×10^6	$(J.kg^{-1})$
Main properties of copper foams and the composite.			
Adsorbent thickness (δ_{coat})	1×10^{-5}		m
Bed permeability (K_p)	10^{-8}		m^2
Bed porosity (ε_b)	0.8		-----
Volume fraction of the copper foam (ζ)	0.52		-----
Copper density (ρ_{copper})	8954		$(kg.m^{-3})$
Specific heat of copper ($C_{p,copper}$)	390		$(J.kg^{-1}.K^{-1})$
Thermal conductivity of copper (k_{copper})	398		$(W.m^{-1}.K^{-1})$
The geometrical and operating parameters of the AHEx.			
Mass of adsorbent in each bed	2		kg
Tube length (L)	0.4		m
Inner radius of the tube (R_i)	0.0045		m
Outer radius of the tube (R_o)	0.005		m
Copper foam thickness (R_c)	0.002		m
Vacuum chamber space(L_{ch})	2		mm
Vapor in / out opening length	8		mm
Average hot water velocity ($u_{ave,hot,in}$)	0.56		$m.s^{-1}$
Average cold water velocity ($u_{ave,cool,in}$)	0.792		$m.s^{-1}$
Hot water temperature ($T_{hw,i}$)	95		^oC
Cold water temperature ($T_{cw,i}$)	30		^oC
Adsorption /desorption time	420/180		sec
Pre-heating/Pre-cooling time	1.6/1.5		sec

Table 2. The geometrical and operating parameters of the condenser and the evaporator.

Operational conditions for condenser		
$\boldsymbol{M_{cond,rl}C_{p,cond,rl} + M_{cond,met}C_{p,cond,met}}$	$2.5 \times 4180 + 12 \times 386$	$J.K^{-1}$
$\boldsymbol{UA_{cond}}$	4114×1.855	$W.K^{-1}$
$\boldsymbol{\dot{m}_{cw}C_{p,cw}}$	0.6271×4180	$W.K^{-1}$
$\boldsymbol{T_{cw,i}}$	30	^oC
Condenser initial temperature ($\boldsymbol{T_{cond,init}}$)	30	^oC
Operational conditions for evaporator		
$\boldsymbol{M_{eva,rl}C_{p,eva,rl} + M_{eva,met}C_{p,eva,met}}$	$20 \times 4180 + 4.45 \times 386$	$J.K^{-1}$
$\boldsymbol{UA_{eva}}$	2557×0.6	$W.K^{-1}$
$\boldsymbol{\dot{m}_{chw}C_{p,chw}}$	0.4240225×4180	$W.K^{-1}$
$\boldsymbol{T_{chw,i}}$	14.8	^oC
Evaporator initial temperature ($\boldsymbol{T_{evap,init}}$)	14.8	^oC

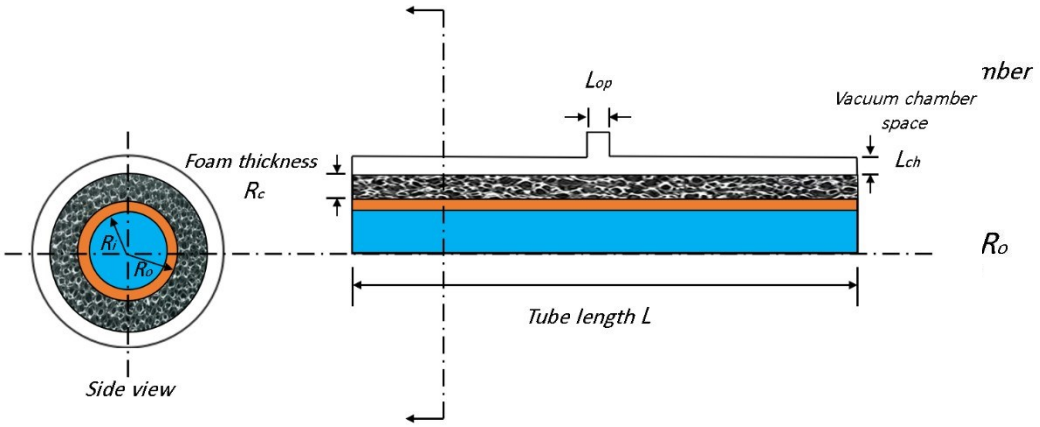

Fig. 4. Schematic diagram of a single foamed adsorption tube to indicate dimensions' labels.

3.4 Initial and boundary conditions

The performance indicators were calculated when the cyclic numerical results stabilized to ensure that the system's performance was independent of the initial conditions, often after five cycles. The boundary conditions adopted in the CFD model solution are populated in **Table 3**.

Table 3. Boundary conditions of the investigated 2-D axisymmetric numerical model

	Pre-heating	Desorption	Precooling	Adsorption
Axisymmetric axis	$\frac{\partial T_f}{\partial r}\Big\vert_{r=0} = 0$ & $\frac{\partial u_f}{\partial r}\Big\vert_{r=0} = 0$			
HTF inlet	$T_f\vert_{z=0} = T_{hw,i}$ $u_z = u_{ave,hot,in}$ $u_r = 0$		$T_f\vert_{z=0} = T_{cw,i}$ $u_z = u_{ave,cool,in}$ $u_r = 0$	
HTF outlet	$\frac{\partial T_f}{\partial z}\Big\vert_{z=L} = 0$ & $p_f = P_{atm}$			
Valve opening	Insulated	$\frac{\partial T}{\partial r} = 0$	Insulated	$T_v = T_{eva}$
	No-slip	$p = P_{cond}$	No-slip	$p = P_{eva}$

3.5 Numerical solution procedures

The aforementioned governing equations and the boundary conditions were defined in COMSOL Multiphysics using six physics to be numerically discretized and solved in a time-dependent fully-coupled model manner. Heat Transfer Physic was solved for the temperature in all domains as a conjugate heat transfer problem. Turbulent Flow (K - ε) Physics was solved for the fluid flow and turbulence model parameters in HTF inside the bed tubes. Free and Porous Media Flow Physics was adopted to solve the mass and the momentum transport equations for both composited foam-adsorbent and vacuum chamber domains and coupled the flow at the interface between them. Convection–Diffusion Equation Physic was used for representing the LDF model. Two Ordinary Differential Equations were adapted to apply the condenser and the evaporator equations at the valve openings' boundary conditions. All source terms, including the partial differential equations and the temperature-dependent thermophysical properties, are integrated with the above physics using user-defined variables.

A time-dependence study was conducted, and all the equations were solved by applying the segregated approach and using the PARDISO and MUMPS solvers to get the best converge. The maximum time step ranged from 0.001 s to 0.1 s for pre-heating and pre-cooling phases where variables could have sharp changes and from 0.1 s to 1 s for adsorption and desorption phases where the main variables have stepper or minor changes.

A physics-controlled option in the COMSOL mesh builder was employed. Therefore, boundary mesh layers in different domains were built to consider the high gradients in the variables solved at these boundaries with appropriate growth rates. In this builder, an extra-fine mesh option was chosen with total mesh elements (506664) for the foam thickness of 2 mm. Mesh independence study showed good accuracy with maximum changes of 0.14% in the calculated COP and SCP. The average element quality was 0.8591, and the maximum growth rates in the boundary mesh elements of the thermal fluid domain and the adsorbent and vacuum chamber domains were 1.08 and 1.1, respectively.

4 Results and discussion

4.1 Validation

The available data on copper foam coated with CPO-27(Ni) and SAPO-34 reported by Pinheiro et al. [31] was used to validate the developed model. The model for validation was undertaken on a single bed adsorption heat pump with a regeneration temperature of 95 °C, adsorption temperature of 35 °C, condensation pressure of 5624 Pa and evaporation pressures of 870 Pa. As shown in Fig. 5, the developed model was in good agreement with the published data by Pinheiro et al. [31]. Generally, the effect of different mass transfer mechanisms is more prominent during the adsorption and desorption processes, particularly at lower pressures during the adsorption process [45]. The present numerical model considered the modified Navier-Stokes equations in modeling the momentum balance effect on the vapor transport in the foam-based adsorbent domain. It included the inertia and viscous effects besides the permeability effect, which is not the case when Darcy's law was considered in Ref. [31]. However, the differences in uptakes were within the acceptable range with a maximum of 0.006 $kg_w.kg_{ads}^{-1}$ at a time of 360 s, as shown in Fig. 5 c.

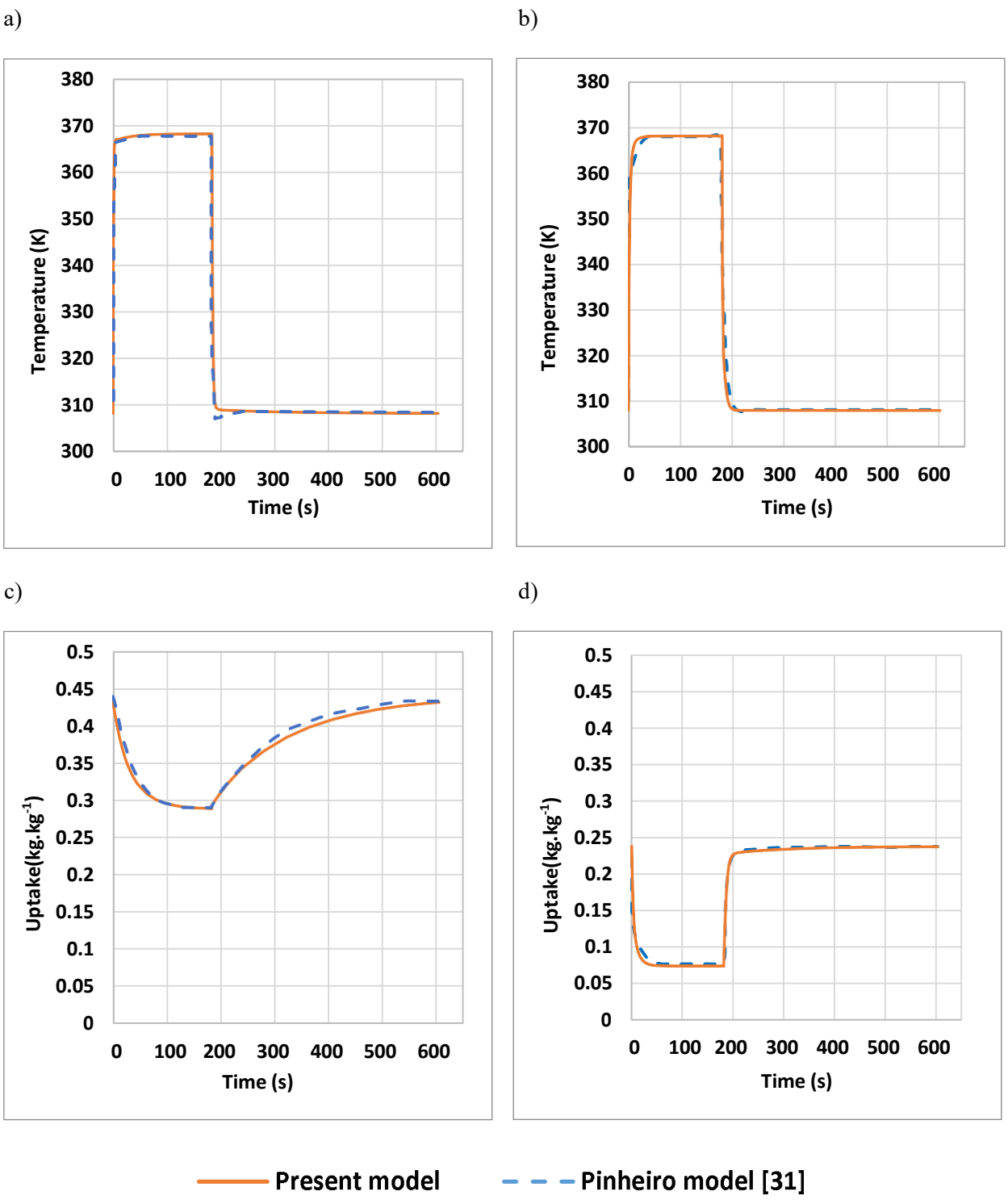

Fig. 5. Comparison between the time variations of the temperatures and uptakes obtained from the present model and those obtained from reference [31]: (a)&(c) for CPO-27 (Ni); and (b)&(d) for SAPO-34.

4.2 Cycle time

The baseline model consists of 2 beds, each constructed from plain tubes covered by a 2 mm adsorbent-coated copper foam layer. The cycle time was 600 sec:180 s for desorption and 420 s for adsorption; and benchmarked against 180s cycle time: 90 s for desorption and 90 s for adsorption. Fig. 6 shows the average temperature, pressure, and uptake for two adsorbent materials during adsorption/desorption processes: CPO-27(Ni) and

SAPO-34. Although both materials' adsorption and desorption temperatures were the same, the SAPO-34 coated bed showed higher adsorption/desorption uptake/offtake in a shorter time due to its higher kinetics, as its mass transfer coefficient is higher than that for CPO-27(Ni) by two orders of magnitude [31]. In addition, the pressure spikes up to 10840 Pa, and the corresponding fast uptake/offtake at the beginning of desorption/desorption processes reflects the higher adsorption kinetics of SAPO-34.

Fig. 7 and Fig. 8 show the bed uptake during desorption and adsorption modes at different times for the two materials at 10 mm copper foam thickness to be more prominent. The effective thermal conductivity enhancement due to using the copper foam leads to an almost equal and uniform distribution of the uptake in the adsorbent domains of both materials at any specified time during desorption and adsorption phases. However, the higher kinetic performance of the SAPO-34 leads to more shortening of the time required to reach its upper uptake limits in the SAPO-34 based foamed beds compared to CPO-27(Ni) based foamed beds.

The cyclic performance indicators are furnished in Table 4. Despite the outperforming adsorption kinetics of SAPO-34, its cyclic performance was substantially lower than that for CPO-27(Ni) for the cycle time of 600 s. The low COP for SAPO-34 was attributed to the excessive adsorbed heat in the metal mass while the uptake profiles plateaued. For better-utilizing SAPO-34, reducing the cycle time by 70 % enhanced its COP by 163 %, outperforming CPO-27(Ni) by 16.5 %. On the other hand, shortening the cycle time enhanced its SCP by 223 % and specific daily water production (SDWP) by 228 %. Compared to CPO-27(Ni), its SCP and SDWP were 42 % and 43 % higher. Fig. 9 shows the cyclic uptake for both materials at the investigated cycle times. However, the cyclic uptake for CPO-27(Ni) and SAPO-34 are nearly 0.21 kg_w/kg_{ads}, CPO-27(Ni) experienced more hysteresis during the adsorption process due to lower mass transfer coefficient; this negatively affects the energy conversion at the component level. The hysteresis during the adsorption process showed more impact in the case of 180 s cycle time, owing to the insufficient time to maintain the developed pressure potential hence maintaining a satisfactory mass transfer during the desorption/condensation. Given that the comparison between 180s and 600s cycle times explained the influence of mass transfer coefficient on the adsorbent-bed performance, additional cycle times in between would not add to the knowledge and would be at the expense of computational cost.

Table 4. The performance indicators of the systems at 180 and 600 s cycle times

Cycle time	CPO-27(Ni)		SAPO-34		Units
	600 s	180 s	600 s	180 s	
COP	0.112	0.104	0.046	0.121	[-]
SCP	832	1182	793	2561	$W.kg^{-1}$
SDWP	29.5	42	28	92	$m^3.ton^{-1}.day^{-1}$

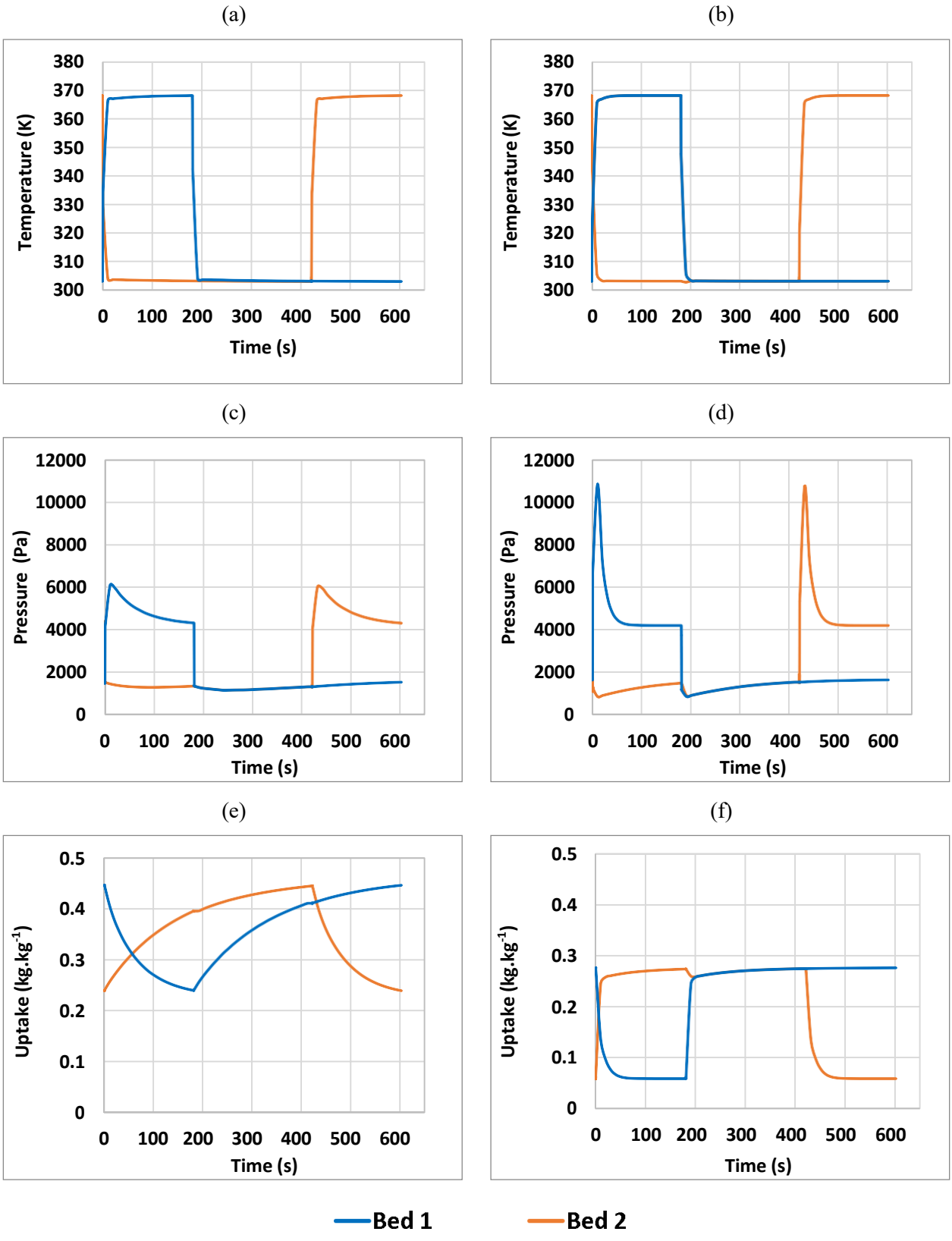

Fig. 6.The time variations of average temperature, pressure and uptake in the two beds: (a), (c), and (e) for CPO-27 (Ni); (b),(d),and (f) for SAPO-34

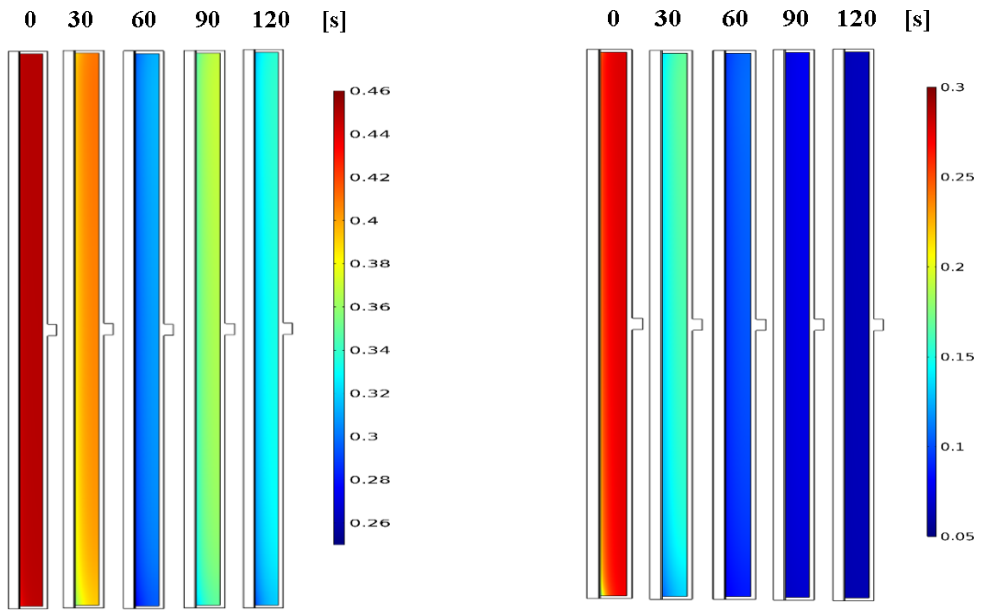

(a) (b)

Fig. 7. Bed uptakes at different times during the desorption mode: (a) CPO-27 (Ni); (b) SAPO-34

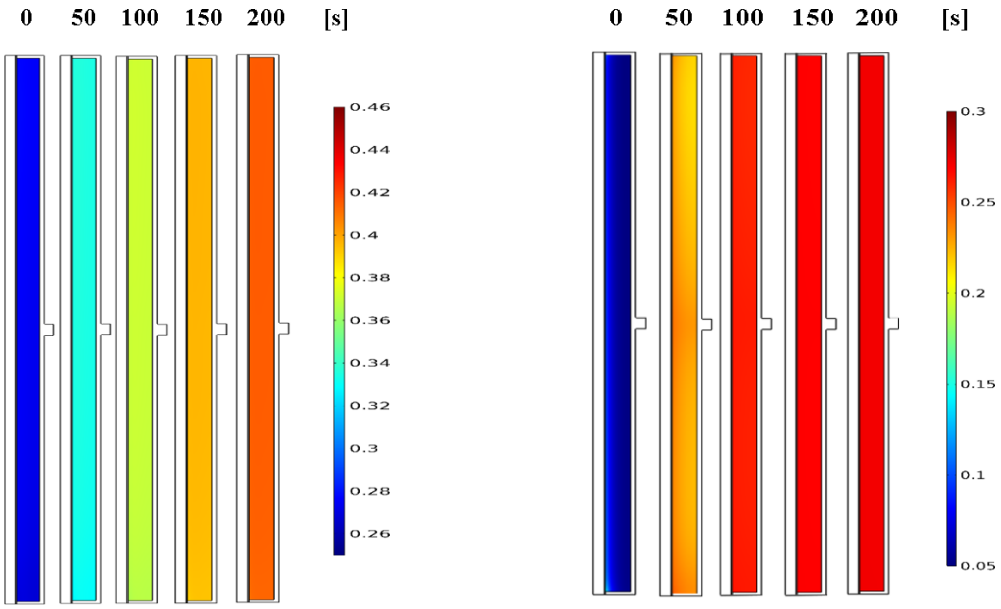

(a) (b)

Fig. 8. Bed uptakes at different times during the adsorption mode: (a) CPO-27 (Ni); (b) SAPO-34

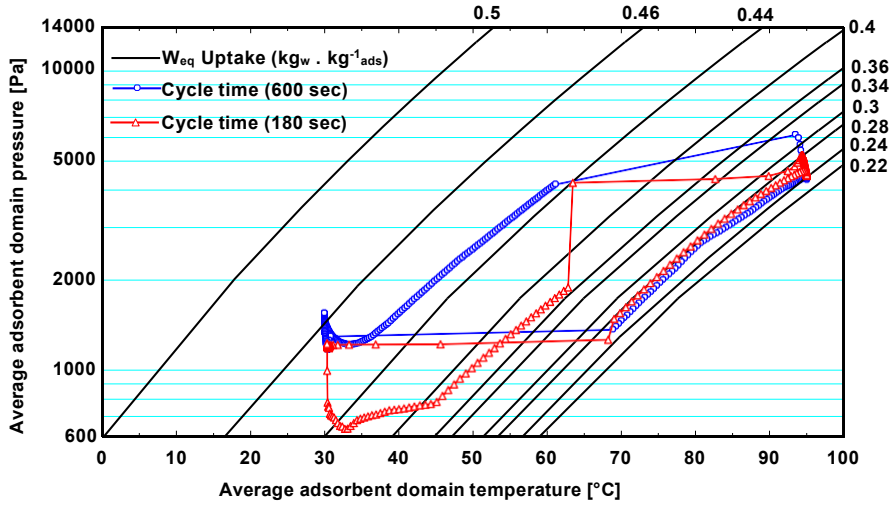

(a)

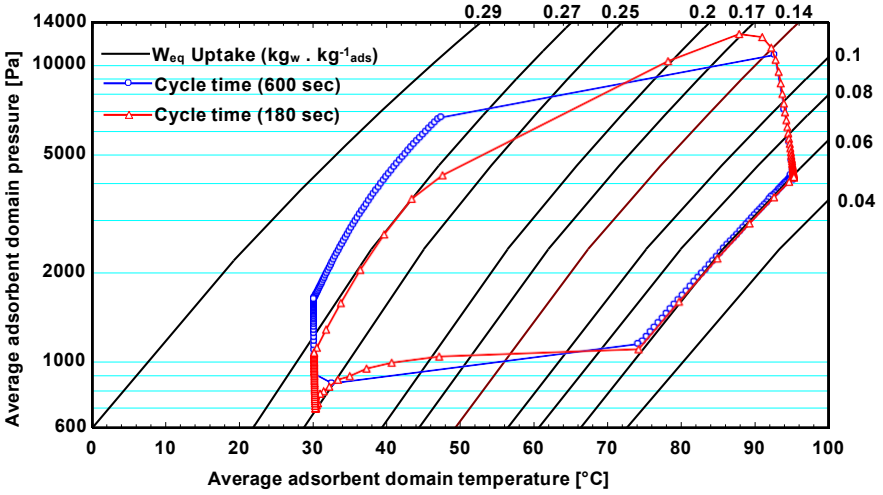

(b)

Fig. 9. The P-T-W_{eq} diagram at cycle times 180 s and 600 s: (a) CPO-27 (Ni); (b) SAPO-34

4.3 Metal foam thickness

The thickness of copper foam varied from 2 mm to 15 mm while maintaining the adsorbents' mass constant by adjusting the number of the tubes, as shown in Table 5. The cycle time was fixed at 600s. Increasing the metal foam's thickness increased the thermal mass of the adsorbent bed, essentially due to increasing the total metal mass to the adsorbent mass. The increased thermal mass prolonged the adsorbent bed's thermal response, reducing the cyclic water uptake, as shown in Fig.10. The accumulated effect of the poor thermal response at large foam thickness and the low mass transfer coefficient of CPO-27(Ni) slowed its dynamic thermal response hence the mass transfer response. Besides, increasing the thickness of the metal foam increased the hysteresis during the adsorption process associated with the CPO-27(Ni) coated bed, as shown in Fig. 11.

Despite the poor adsorbent bed's thermal response at larger foam thicknesses and the subsequent slowed uptake benefitted the magnitude of cyclic uptake to prolonged heating/cooling during desorption/adsorption processes. In general, the COPs of both foam-based systems are considerably enhanced at larger foam

thicknesses. However, SCPs and SDWPs in the SAPO-34 system are almost similar, and in the CPO-27(Ni) system gradually reduced with increasing the foam thickness. It is due to narrowing the range of the effective uptake for CPO-27(Ni) by increasing the foam thickness, as the minimum uptake was highly influenced by increasing the foam thickness. At the same time, the maximum uptake was slightly changed, as shown in Fig. 11. It results from the poor mass transfer at higher foam thickness, at the component level, due to the delayed thermal response of the adsorbent bed combined with the mass transfer coefficient at the material level. On the other hand, both minimum and maximum uptake for the SAPO- 34 were marginally influenced by increasing the thickness due to the relatively higher mass transfer coefficient, which compensated for the low thermal response at higher foam thicknesses.

The significance of adsorption hysteresis in CPO-27(Ni) coated bed and its impact on the energy conversion at the adsorbent-bed level can be quantified by 9.3% higher COP in SAPO-34 coated bed at 15 mm foam thickness, as shown in Fig. 12-a. The relative increase of the cyclic water uptake led to higher SCP and SDWP at smaller foam thicknesses. Although larger foam thicknesses tend to slow the adsorption/desorption process, it might benefit the applications that require long cycle times. As illustrated in Fig. 12(d), by increasing the copper foam thickness, VCP increased until it reached its maximum of 154.7 W. L^{-1} in CPO-27(Ni) coated bed at 10 mm copper foam thickness and 162 W. L^{-1} in SAPO-34 coated bed at 15 mm copper foam thickness.

The percentage changes of the cyclic performance indicators compared to the base cases of 2 mm thickness are furnished in Table 6; this to demonstrate the above-explained combined effect of the heat and mass transfer performance at the material and adsorbent-bed levels over a range of foam thicknesses on the overall system's performance. Positive effects are noticed in all SAPO-34 coated bed system indicators at foam thickness higher than 2 mm, which leads to choosing the SAPO-34 coated bed system over the CPO-27(Ni)-coated-bed system for ACD system applications.

Table 5. The number of tubes per bed at each foam thickness

Foam thickness	2 mm	5 mm	10 mm	15 mm
N_{tube} CPO_27(Ni)	266	85	32	17
N_{tube} SAPO-34	306	98	37	20

Table 6. The percentage change in the COP, SCP, SDWP and VCP at each foam thickness compared to 2 mm thickness.

Foam thickness	2 mm	5 mm	10 mm	15 mm
CPO_27(Ni)				
% Change in COP	0	148.5	267	287
% Change in SCP	0	-6	-16	-32
% Change in SDWP	0	-9	-16	-33
% Change in VCP	0	44	52	30
SAPO-34				
% Change in COP	0	449	766	924
% Change in SCP	0	5	5.4	2.7
% Change in SDWP	0	5.3	6	3
% Change in VCP	0	61	90	93

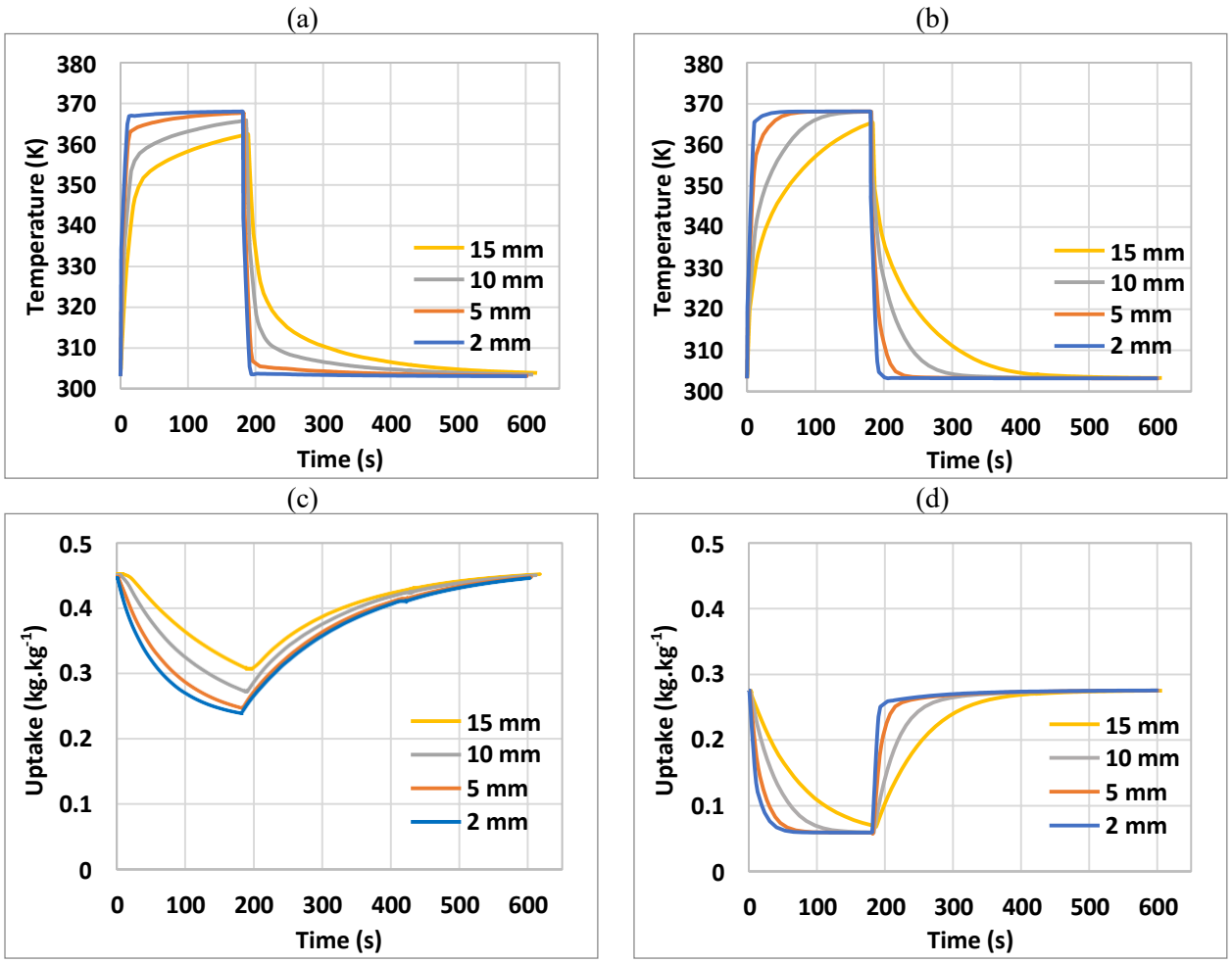

Fig.10. Effect of copper foam thickness on average bed temperature and average bed uptake: (a), (c) for CPO-27 (Ni); (b),(d) for SAPO-34

(a)

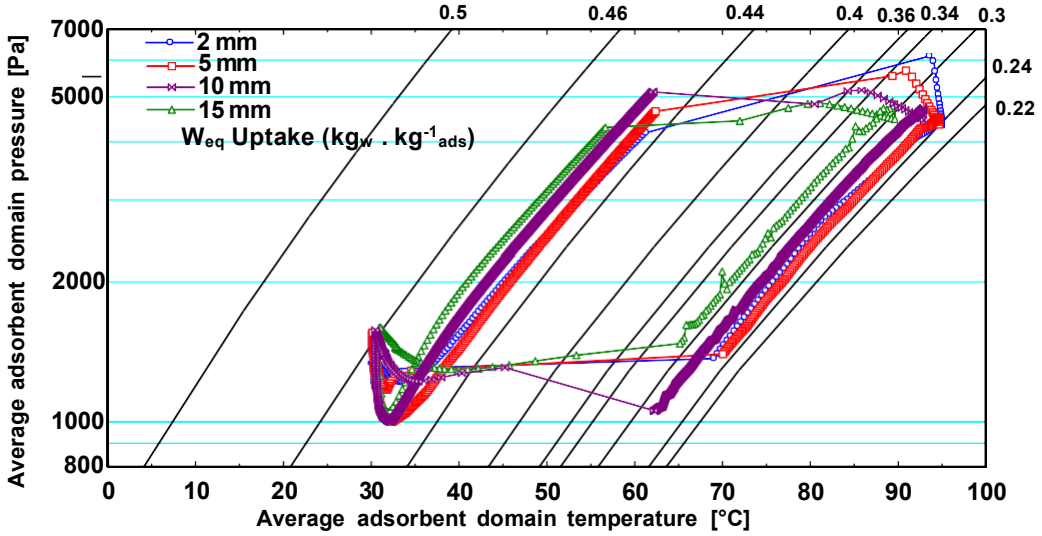

(b)

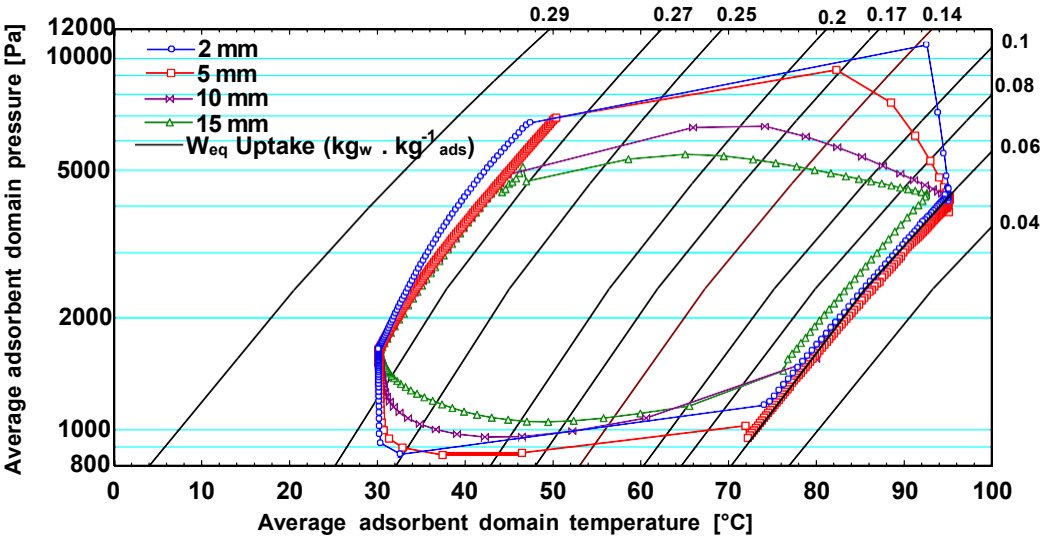

Fig. 11. P-T-W_{eq} under different copper foam thicknesses; (a) CPO-27 (Ni); (b) SAPO-34.

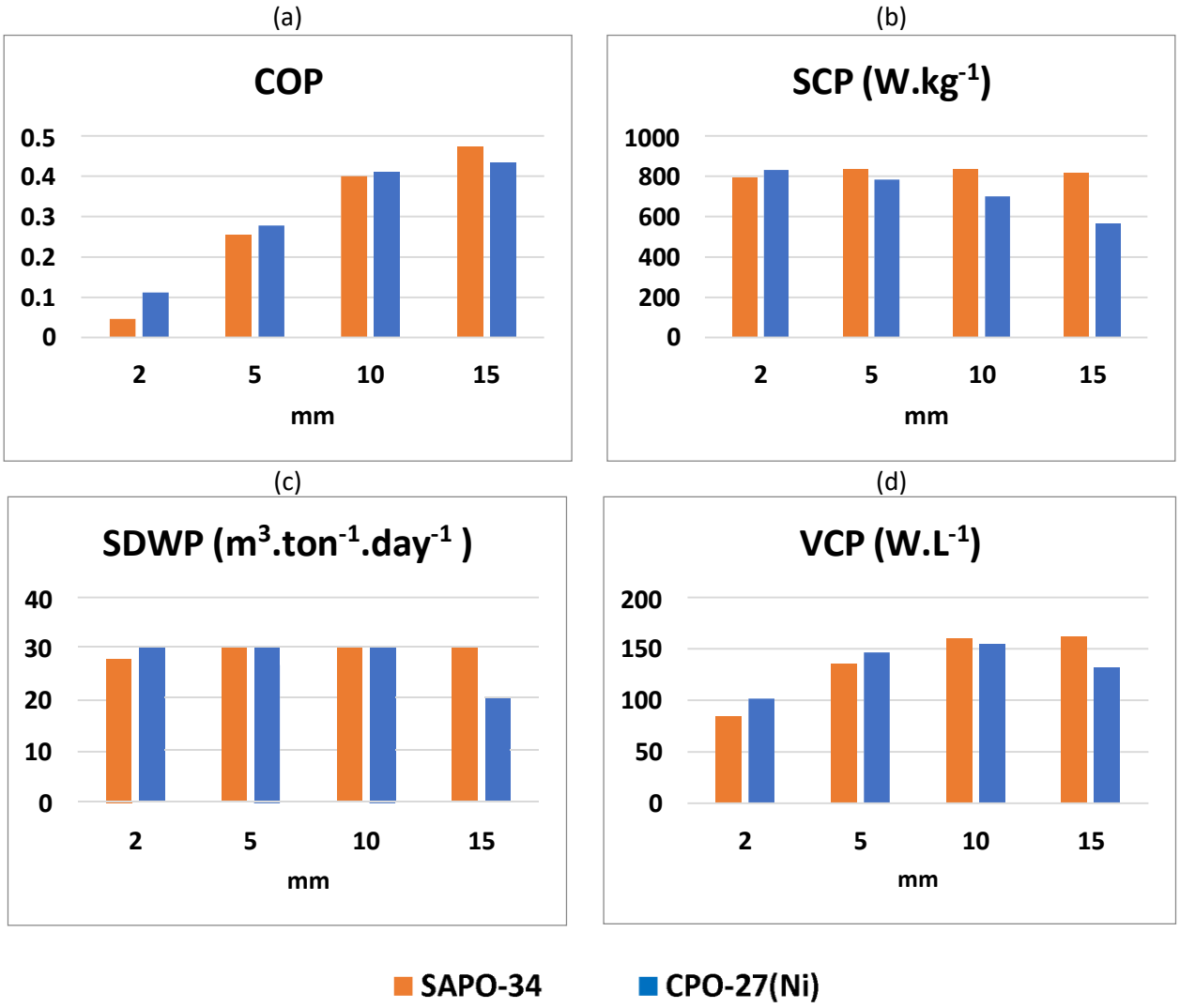

Fig. 12. Effect of copper foam thickness on: (a) COP; (b) SCP; (c) SDWP; (d) VCP.

4.4 The effect of adsorption and regeneration temperatures

Fig. 13 shows the effect of adsorption and regeneration temperatures on the system performance: COP, SCP, SDWP, and VCP. The cooling water inlet temperature ranged between 25-40 °C, the regeneration temperature ranged between 70-100 °C, the chilled water inlet temperature was fixed at 14.8 °C, and the coating thickness was 10 mm. Changing the regeneration temperature was more significant in CPO-27 (Ni) over the investigated range. For CPO-27 (Ni) at 25 °C cooling water inlet temperature, the COP increased by 72 % by increasing the regeneration temperature from 70 °C to 100 °C. For SAPO-34, the effect of the regeneration temperature is more noticeable at 40 °C cooling inlet temperature at which the COP changed and increased by 42.6 % by increasing the regeneration temperature from 70 °C to 100 °C. At 25, 30, and 35 °C cooling water inlet temperature, the COP was nearly constant while varying the regeneration temperature. SAPO-34 coated bed showed relatively higher COP at regeneration temperature below 90 °C but less COP at higher regeneration temperature; this is attributed to the excessive heat stored in the thermal mass due to the prolonged cycle time that negates the positive effect of increasing the cyclic temperature lift.

For both materials, the SCP, SDWP, and VCP were increased by increasing the regeneration temperature simultaneously with reducing the cooling water inlet temperature due to increasing the amounts of adsorbate cyclic uptake/offtake [53]. On the one hand, the values of SCP, SDWP, and VCP for SAPO-34 were higher than those for CPO-27 (Ni) for the given regeneration and cooling water inlet temperature ranges, except for 100 °C regeneration temperature and 25 °C cooling water inlet temperature, the CPO-27 (Ni) coated bed outperformed SAPO-34 coated bed. On the other hand, the CPO-27 (Ni) coated bed exhibited steeper change by increasing the regeneration temperature with strong potential of outperforming SAPO-34 coated bed at excessively high regeneration temperature simultaneously with low cooling water inlet temperature, as the cycle time was long enough to circulate more significant amounts of the adsorbate. CPO-27 (Ni) coated bed showed 345% enhancement in the performance (229 - 1016 $W.kg^{-1}$ SCP, 8 - 36 $m^3ton^{-1}day^{-1}$ SDWP, and 51 - 225 WL^{-1} VCP) by increasing the regeneration temperature from 70 °C to 100 °C, while SAPO-34 showed 79% enhancement in the performance (537 - 962 $W.kg^{-1}$ SCP, 19 - 34 $m^3.ton^{-1}.day^{-1}$ SDWP and 103 - 184 $W.L^{-1}$ VCP) within the same temperature ranges.

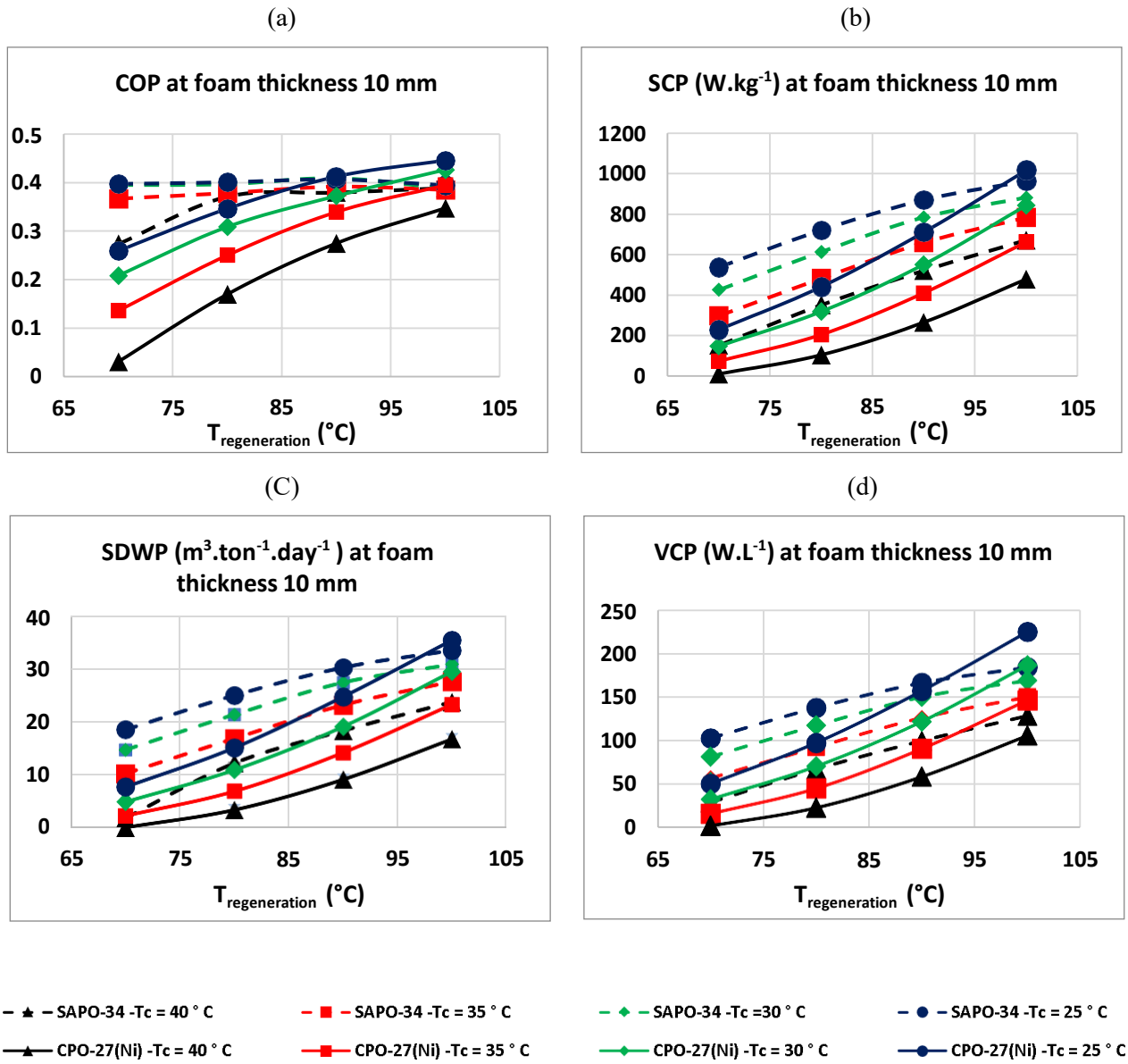

Fig. 13. Effect of changing inlet regeneration temperatures at different inlet cooling water temperatures on COP, SCP, SDWP and VCP of both systems.

4.5 The effect of chilled water and regeneration

Fig. 14 shows the effect of chilled water and regeneration temperatures on the system performance: COP, SCP, SDWP, and VCP. The chilled water inlet temperature ranged between 11-17 °C, the regeneration temperature ranged between 70-100 °C, the cooling water inlet temperature was fixed at 30 °C, and the coating thickness was 10 mm. Despite chilled water inlet temperature being a crucial parameter and a strong function of the desired cooling load, directly linked to the ambient conditions, its implication in the system performance was marginal compared to the regeneration temperature. Generally, the influence of the regeneration temperature was more significant in CPO-27 (Ni) than that in SAPO-34.

The COP for CPO-27 (Ni) increased by 110% (averagely 0.2 - 0.421), while it increased by 2.6% for SAPO-34 (averagely 0.378 - 0.388) by increasing the regeneration temperature from 70 °C to 100 °C and for the investigated chilled water temperature range. The SCP, SDWP, and VCP for CPO-27 (Ni) increased by 524%

(averagely 132 - 821 W.kg^{-1}, 4.7 - 29.3 m^3.ton^{-1}.day^{-1}, and 29 - 181.5 W.L^{-1}), while it increased by 118% for SAPO-34 (averagely 393 - 855 W.kg^{-1}, 14 - 31 m^3.ton^{-1}.day^{-1} and 75 - 163.4 W.L^{-1}) by increasing the regeneration temperature from 70 °C to 100 °C and for the investigated chilled water temperature range. Table 7 shows the effect of decreasing cycle time from 600 s to 180 s on the performance of adsorption systems when coated with the two materials at 10 mm copper foam thickness. Reducing cycle time affects the average cyclic performance indicators, especially for SAPO-34 coated bed, but the COP decreased by 34 % for CPO-27 (Ni) coated bed.

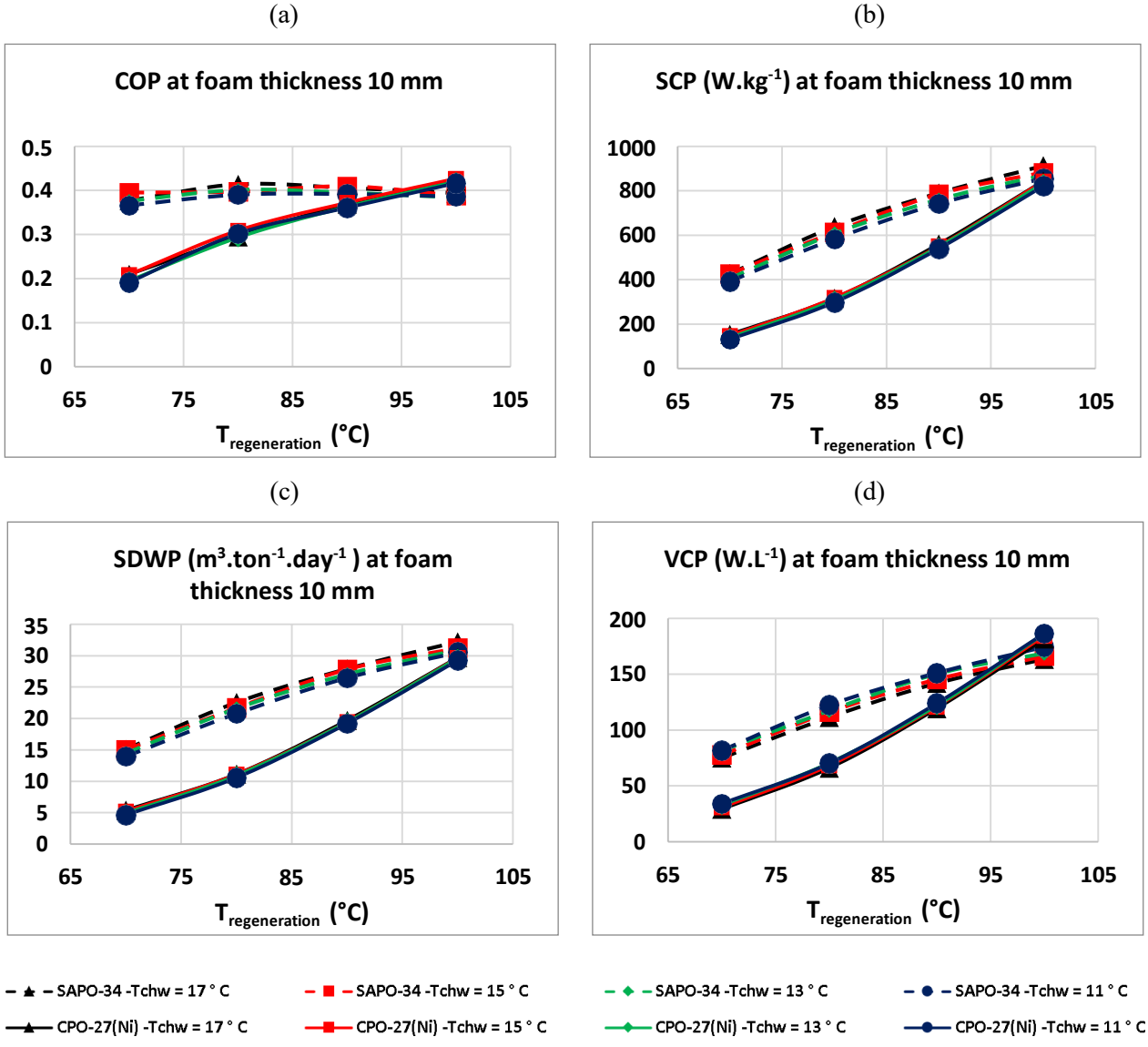

Fig. 14. Effect of changing inlet regeneration temperatures at different inlet chilled water temperatures on COP, SCP, SDWP and VCP of both systems.

Table 7. Values of the cyclic performance indicators for both adsorbent systems at cycle times of 600 s and 180 s, and using 10 mm copper foam thickness.

	Cycle time (s)	COP	SCP ($W.kg^{-1}$)	SDWP ($m^3.ton^{-1}.day^{-1}$)	VCP ($W.L^{-1}$)
CPO-27 (Ni)	600 (420,180)	0.41	700	25	155
	180 (90,90)	0.277	924	32.5	204
SAPO-34	600 (420,180)	0.41	836	30	160
	180 (90,90)	0.4	2258	81	432

5 Conclusion

This paper aimed to undertake a comparative study between copper foamed beds coated with CPO-27(Ni) and SAPO-34 adsorbents as the most promising materials for hybrid cooling and desalination. The results indicated a considerable enhancement in the system performance compared to the conventional adsorbents and significant impacts of operational conditions and foam thickness of both adsorbents on the system performance, which was not revealed in the open literature for adsorption cooling and desalination systems. Therefore, it can be concluded that:

- Shortening the cycle time from 600 s to 180 s positively impacted the system performance, specifically in foam beds coated with SAPO-34. The COP, SCP, and SDWP increased by 163%, 223%, and 228%, respectively. The reduced cycle was better utilizing the outstanding adsorption kinetics of SAPO-34.
- Increasing the copper foam thickness increased the COP for both materials. For the CPO-27 (Ni) coated bed, increasing copper foam thickness decreased the SCP and SDWP from 832 to 563 W.kg-1 and 29.5 to 19.7 $m^3.ton^{-1}.day^{-1}$ respectively; this owing to the slower thermal response hence the delayed mass transfer due to the higher metal thermal mass in the adsorbent bed. However, a minimal change was reported in SAPO-34 coated bed.
- Although changing the chilled water inlet temperature showed a marginal effect on the performance of the two materials, increasing the regeneration temperature was more significant, especially for the CPO-27 (Ni) coated bed. For CPO-27 (Ni) coated bed, the enhancement was 110% for COP and 524% for SCP, SDWP, and VCP. For the SAPO-34 coated bed, the enhancement was 2.6 % for COP and 118 % for SCP, SDWP, and VCP.
- Whilst SAPO-34 coated bed generally outperformed the CPO-27 (Ni) coated bed because of the faster mass transfer performance, the rate of increasing the cyclic performance for the CPO-27 (Ni) coated bed was steeper than SAPO-34.

Acknowledgements

This work was supported by King Saud University, Deanship of Scientific Research, and College of Engineering Research Center.

References

1. Sachs, J., et al., *Clustered spatially and temporally resolved global heat and cooling energy demand in the residential sector.* Applied Energy, 2019. **250**: p. 48-62.
2. Saha, B.B., et al., *Fundamental and application aspects of adsorption cooling and desalination.* Applied Thermal Engineering, 2016. **97**: p. 68-76.
3. Teo, H.W.B., et al., *Experimental study of isotherms and kinetics for adsorption of water on Aluminium Fumarate.* International Journal of Heat and Mass Transfer, 2017. **114**: p. 621-627.
4. Pinheiro, J.M., et al., *Adsorption heat pump optimization by experimental design and response surface methodology.* Applied Thermal Engineering, 2018. **138**: p. 849-860.
5. Denzinger, C., et al., *Toward sustainable refrigeration systems: Life cycle assessment of a bench-scale solar-thermal adsorption refrigerator.* International Journal of Refrigeration, 2021. **121**: p. 105-113.
6. Elsheniti, M.B., et al., *Performance of a solar adsorption cooling and desalination system using aluminum fumarate and silica gel.* Applied Thermal Engineering, 2021. **194**: p. 117116.
7. Han, B. and A. Chakraborty, *Advanced cooling heat pump and desalination employing functional UiO-66 (Zr) metal-organic frameworks.* Energy Conversion and Management, 2020. **213**.
8. *Graf*, S., et al., *Toward Optimal Metal–Organic Frameworks for Adsorption Chillers: Insights from the Scale-Up of MIL-101(Cr) and NH2 -MIL-125.* Energy Technology, 2019. **8**(1).
9. Shi, Z., et al., *Machine learning and in silico discovery of metal-organic frameworks: Methanol as a working fluid in adsorption-driven heat pumps and chillers.* Chemical Engineering Science, 2020. **214**.
10. Ghazy, M., A.A. Askalany, and B.B. Saha, *Maxsorb III/HFC404a as an adsorption pair for renewable energy driven systems.* International Journal of Refrigeration, 2020. **120**: p. 12-21.
11. Tso, C.Y., et al., *Experimental performance analysis on an adsorption cooling system using zeolite 13X/CaCl2 adsorbent with various operation sequences.* International Journal of Heat and Mass Transfer, 2015. **85**: p. 343-355.
12. Kulakowska, A., et al., *Effect of Metal and Carbon Nanotube Additives on the Thermal Diffusivity of a Silica Gel-Based Adsorption Bed.* Energies, 2020. **13**(6): p. 1391.
13. Askalany, A.A., et al., *Effect of improving thermal conductivity of the adsorbent on performance of adsorption cooling system.* Applied Thermal Engineering, 2017. **110**: p. 695-702.
14. Demir, H., M. Mobedi, and S. Ülkü, *The use of metal piece additives to enhance heat transfer rate through an unconsolidated adsorbent bed.* International Journal of Refrigeration, 2010. **33**(4): p. 714-720.
15. Mikhaeil, M., M. Gaderer, and B. Dawoud, *On the development of an innovative adsorber plate heat exchanger for adsorption heat transformation processes; an experimental and numerical study.* Energy, 2020. **207**.
16. White, J., *CFD Simulation and Experimental Analyses of a Copper Wire Woven Heat Exchanger Design to Improve Heat Transfer and Reduce the Size of Adsorption Beds.* Computation, 2016. **4**(1).
17. Saleh, M.M., et al., *Wire fin heat exchanger using aluminium fumarate for adsorption heat pumps.* Applied Thermal Engineering, 2020. **164**.
18. Zhu, L.Q., et al., *Experimental investigation on composite adsorbent – Water pair for a solar-powered adsorption cooling system.* Applied Thermal Engineering, 2018. **131**: p. 649-659.
19. Calabrese, L., et al., *New SAPO-34-SPEEK composite coatings for adsorption heat pumps: Adsorption performance and thermodynamic analysis.* Energy, 2020. **203**: p. 117814.
20. Lee, J.-G., K.J. Bae, and O.K. Kwon, *Performance Investigation of a Two-Bed Type Adsorption Chiller with Various Adsorbents.* Energies, 2020. **13**(10): p. 2553.
21. Albaik, I., et al., *A comparison between the packed and coated finned tube for adsorption system using aluminium fumarate: Numerical study.* Thermal Science and Engineering Progress, 2021. **22**: p. 100859.

22. Freni, A., et al., *Zeolite synthesised on copper foam for adsorption chillers: A mathematical model.* Microporous and Mesoporous Materials, 2009. **120**(3): p. 402-409.
23. Duong, X.Q., et al., *Effect of coating thickness, binder and cycle time in adsorption cooling applications.* Applied Thermal Engineering, 2021. **184**.
24. Calabrese, L., et al., *Synthesis of SAPO-34 zeolite filled macrocellular foams for adsorption heat pump applications: A preliminary study.* Applied Thermal Engineering, 2017. **124**: p. 1312-1318.
25. Calabrese, L., et al., *Adsorption performance and thermodynamic analysis of SAPO-34 silicone composite foams for adsorption heat pump applications.* Materials for Renewable and Sustainable Energy, 2018. **7**(4).
26. Schnabel, L., et al., *Adsorption kinetics of zeolite coatings directly crystallized on metal supports for heat pump applications (adsorption kinetics of zeolite coatings).* Applied Thermal Engineering, 2010. **30**(11-12): p. 1409-1416.
27. Hua, L.J., et al., *Graphic general solutions for desiccant coated heat exchangers based on dimensional analysis.* International Journal of Heat and Mass Transfer, 2020. **154**: p. 119654.
28. Bonaccorsi, L. and E. Proverbio, *Synthesis of thick zeolite 4A coatings on stainless steel.* Microporous and Mesoporous Materials, 2004. **74**(1-3): p. 221-229.
29. Calabrese, L., et al., *Morphological and functional aspects of zeolite filled siloxane composite foams.* Journal of Applied Polymer Science, 2018. **135**(2).
30. Piperopoulos, E., et al., *Morphological and Structural Evaluation of Hydration/Dehydration Stages of MgSO4 Filled Composite Silicone Foam for Thermal Energy Storage Applications.* Applied Sciences, 2020. **10**(2): p. 453.
31. Pinheiro, J.M., et al., *Copper foam coated with CPO-27(Ni) metal–organic framework for adsorption heat pump: Simulation study using OpenFOAM.* Applied Thermal Engineering, 2020. **178**.
32. Calabrese, L., V. Brancato, and A. Frazzica, *Experimental evaluation of the hydrothermal stability of a silicone/zeolite composite foam for solar adsorption heating and cooling application.* Journal of Applied Polymer Science, 2019. **137**(4).
33. Bauer, J., et al., *Zeolite/aluminum composite adsorbents for application in adsorption refrigeration.* International Journal of Energy Research, 2009. **33**(13): p. 1233-1249.
34. Calabrese, L., et al., *Modified Silicone-SAPO34 Composite Materials for Adsorption Thermal Energy Storage Systems.* Applied Sciences, 2020. **10**(23).
35. Bonaccorsi, L., et al., *Synthesis of SAPO-34 on graphite foams for adsorber heat exchangers.* Applied Thermal Engineering, 2013. **61**(2): p. 848-852.
36. Xu, Z., et al., *Study on heat transfer and cooling performance of copper foams cured MIL-101 adsorption unit tube.* Energy, 2020. **191**.
37. Hu, P., J.-J. Yao, and Z.-S. Chen, *Analysis for composite zeolite/foam aluminum–water mass recovery adsorption refrigeration system driven by engine exhaust heat.* Energy Conversion and Management, 2009. **50**(2): p. 255-261.
38. Mohammed, R.H., et al., *Performance enhancement of adsorption beds with silica-gel particles packed in aluminum foams.* International Journal of Refrigeration, 2019. **104**: p. 201-212.
39. Kayal, S., S. Baichuan, and B.B. Saha, *Adsorption characteristics of AQSOA zeolites and water for adsorption chillers.* International Journal of Heat and Mass Transfer, 2016. **92**: p. 1120-1127.
40. Freni, A., et al., *Comparative analysis of promising adsorbent/adsorbate pairs for adsorptive heat pumping, air conditioning and refrigeration.* Applied Thermal Engineering, 2016. **104**: p. 85-95.
41. Wei Benjamin Teo, H., A. Chakraborty, and W. Fan, *Improved adsorption characteristics data for AQSOA types zeolites and water systems under static and dynamic conditions.* Microporous and Mesoporous Materials, 2017. **242**: p. 109-117.
42. Al-Dadah, R., et al., *Metal-organic framework materials for adsorption heat pumps.* Energy, 2020. **190**: p. 116356.
43. Shi, B., et al., *CPO-27(Ni) metal–organic framework based adsorption system for automotive air conditioning.* Applied Thermal Engineering, 2016. **106**: p. 325-333.
44. Elsheniti, M.B., et al., *Adsorption Refrigeration Technologies.* 2018.

45. Elsheniti, M.B., M.A. Hassab, and A.-E. Attia, *Examination of effects of operating and geometric parameters on the performance of a two-bed adsorption chiller.* Applied Thermal Engineering, 2019. **146**: p. 674-687.
46. Çağlar, A., C. Yamalı, and D.K. Baker, *Two dimensional transient coupled analysis of a finned tube adsorbent bed for a thermal wave cycle.* International Journal of Thermal Sciences, 2013. **73**: p. 58-68.
47. Yaïci, W. and E. Entchev, *Coupled unsteady computational fluid dynamics with heat and mass transfer analysis of a solar/heat-powered adsorption cooling system for use in buildings.* International Journal of Heat and Mass Transfer, 2019. **144**: p. 118648.
48. Ingham, D.B. and I. Pop, *Transport phenomena in porous media*. 1998: Elsevier.
49. Bruckner, S., et al., *Modeling of Water Adsorption in SAPO-34-Coated Aluminum Foam.* Chemie Ingenieur Technik, 2017. **89**(6): p. 757-764.
50. Klett, J.W., et al., *The role of structure on the thermal properties of graphitic foams.* Journal of Materials Science, 2004. **39**(11): p. 3659-3676.
51. Patton, A., B.D. Crittenden, and S.P. Perera, *Use of the Linear Driving Force Approximation to Guide the Design of Monolithic Adsorbents.* Chemical Engineering Research and Design, 2004. **82**(8): p. 999-1009.
52. Elsayed, A., et al., *Thermal energy storage using metal–organic framework materials.* Applied Energy, 2017. **186**: p. 509-519.
53. Rezk, A.R.M. and R.K. Al-Dadah, *Physical and operating conditions effects on silica gel/water adsorption chiller performance.* Applied Energy, 2012. **89**(1): p. 142-149.